Magnetic properties of lightly doped antiferromagnetic $YBa_2Cu_3O_y$

O. P. Sushkov
School of Physics, University of New South Wales, Sydney 2052, Australia
(Received 30 May 2011; revised manuscript received 2 September 2011; published 28 September 2011)

The present work addresses $YBa_2Cu_3O_y$ at doping below $x = 6\%$ where the compound is a collinear antiferromagnet. In this region $YBa_2Cu_3O_y$ is a normal conductor with finite resistivity at zero temperature. The value of the staggered magnetization at zero temperature is $\approx 0.6\,\mu_B$, the maximum value allowed by spin quantum fluctuations. The staggered magnetization is almost independent of doping. On the other hand, the Néel temperature decays very quickly, from $T_N = 420$ K at $x = 0$ to practically zero at $x \approx 6\%$. The present paper explains these remarkable properties and demonstrates that the properties result from the physics of a lightly doped Mott insulator with small hole pockets. Nuclear quadrupole resonance data are also discussed. The data shed light on mechanisms of stability of the antiferromagnetic order at $x < 6\%$.

DOI: 10.1103/PhysRevB.84.094532 PACS number(s): 74.72.−h, 75.25.−j, 76.75.+i, 78.70.Nx

I. INTRODUCTION

It is well known that cuprates are layered compounds consisting of CuO_2 planes and there are no doubts that the generic physics of cuprates are related to the CuO_2 plane. In spite of the same generic physics, specific properties of cuprates can be very different depending on crystal structure, ways of doping, etc. The goal of the present work is to shed light on the generic physics via understanding the specific properties of lightly doped antiferromagnetic $YBa_2Cu_3O_y$ (YBCO).

Cuprates are essentially doped Mott insulators. It is well established that Mott insulators possess long-range antiferromagnetic (AF) order; therefore one of the generic problems is how the AF order evolves with doping. Another generic problem is the shape of the Fermi surface. Are there small hole pockets as one expects for a very lightly doped Mott insulator, and how does the surface evolve with doping?

Cuprates are intrinsically disordered materials because of mechanisms of doping. Disorder complicates a theoretical analysis of experimental data, usually masking the generic physics. YBCO is probably the least-disordered cuprate in the low-doping regime. In this paper I denote the hole concentration per unit cell of the CuO_2 layer by x; this is the "doping." YBCO is not superconducting below $x \approx 0.06$, where it behaves as a normal conductor with delocalized holes. The zero temperature resistivity remains finite,[1] apart from very weak logarithmic temperature dependence[2,3] expected for weak disorder. The heat conductivity also indicates delocalization of holes.[4] This is very different from $La_{2-x}Sr_xCuO_4$, where holes are localized and hence the compound is an Anderson insulator[5,6] at $x \lesssim 0.15$.[7] Ultimately, at very low doping, $x \lesssim 0.01$, the disorder wins even in YBCO and it also becomes the Anderson insulator.[1] It is helpful to have in mind an approximate empiric formula[1,8]

$$x \approx 0.35(y - 6.20) \tag{1}$$

to relate the doping level x and the oxygen content y in underdoped YBCO at $x \lesssim 0.12$.

The static "staggered" magnetization in YBCO has been recently measured in the μSR experiment.[9] The experimental plot of the zero-temperature magnetization versus doping is shown in Fig. 1 (top). Remarkably the zero-temperature magnetization is almost doping independent up to $x \approx 0.06$ and then it quickly decays. It is known from neutron scattering experiments[10–13] that the static magnetization fully disappears at the quantum critical point (QCP) $x \approx 0.09$, indicating transition to a state without static magnetism. Importantly, the magnetism at $x > 0.06$ is incommensurate, which is why in the first sentence of this paragraph I put "staggered" in quotations. Value of the incommensurate wave vector Q divided by 2π versus doping is plotted in Fig. 2.

While in the collinear antiferromagnetic phase the zero-temperature staggered magnetization is almost independent of doping, and the Néel temperature decays very quickly from $T_N = 420$ K at $x = 0$ to practically zero at $x \approx 6\%$. This is shown in Fig. 1 (bottom), copied from Ref. 9. The present paper explains these puzzling magnetic properties and shows that they are related to small hole pockets of a lightly doped Mott insulator.

One could think that the survival of antiferromagnetism in lightly doped YBCO is similar to the survival of antiferromagnetism in electron-doped cuprates. However, these are very different phenomena. Antiferromagnetism in lightly electron-doped cuprates is a simple effect well understood within the $t - t' - t'' - J$ model. Due to t' and t'' the electron-hole symmetry is violated; therefore, when injected, electrons go to the antinodal points $(\pm\pi,0)$, $(0,\pm\pi)$ (see, e.g., Ref. 17). The structure of the charge-carrier-magnon vertex in the $t - t' - t'' - J$ model is such that the vertex is zero at the antinodal points. Therefore mobile electrons do not frustrate the AF background. This is the mechanism behind survival of antiferromagnetism in electron-doped cuprates up to $x \approx 0.15$, when electrons start to penetrate to the nodal points.[17] Holes, when injected, always go to the nodal points where their interaction with magnons is maximum, frustrating the AF background. Therefore antiferromagnetism of the hole-doped YBCO with mobile holes[18] is a highly nontrivial effect. This effect is addressed in the present work.

$YBa_2Cu_3O_y$ is doped via filling oxygen chains located above the CuO_2 planes. It has been argued that at $y = 6.5$ when every second chain is full, the chain modulation generates the charge density wave (CDW) of in-plane holes.[19,20] Nuclear quadruple resonance (NQR) for in-plane Cu is an excellent local probe of the hole density.[21] Figure 3 shows ^{63}Cu

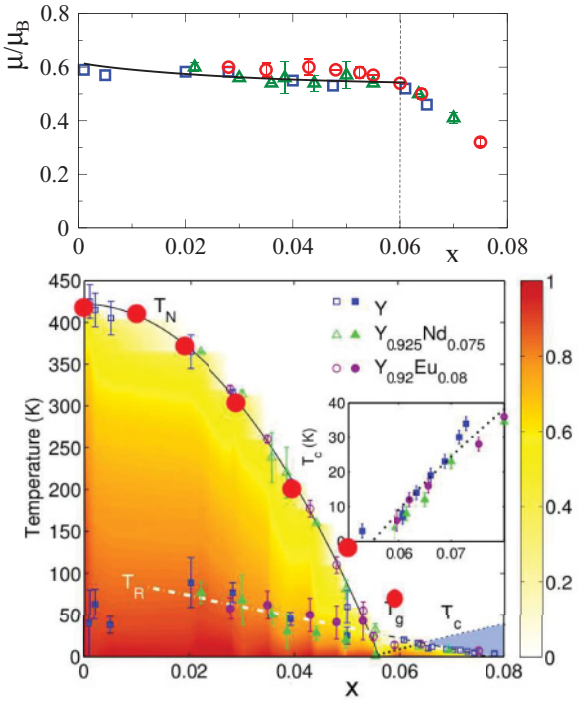

FIG. 1. (Color online) The YBCO μSR data from Ref. 9. Top: Zero-temperature "staggered" magnetization versus doping. The solid line shows results of the present calculations. Bottom: The Néel temperature and the staggered magnetization versus doping. The inset shows the superconducting critical temperature versus doping. Large red dots show the Néel temperature calculated in the present work.

NQR frequency sweeps from Ref. 22 for several values of oxygen content. There is a single narrow line at about optimal doping $y \approx 7$ indicating a very homogeneous hole density corresponding to completely filled chains. On the other hand, at $y \approx 6.5$ there are two distinct lines indicating a bimodal hole density distribution, in agreement with Refs. 19 and 20. Importantly, the bimodal distribution is evident even at lower doping, $y = 6{,}4{,}6.45$, indicating the CDW induced by the oxygen chain superstructure. Below $y = 6.5$ the NQR lines are broader compared to $y = 6.5$. This is because the

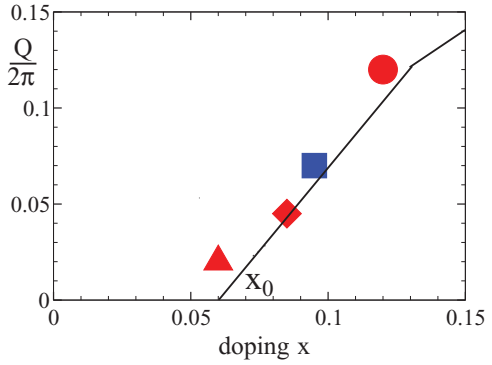

FIG. 2. (Color online) Incommensurate wave vector versus doping. The blue square,[14] the red circle,[10] the red diamond,[12] and the red triangle[15] show neutron-scattering data. The solid line shows the theoretical value.[16]

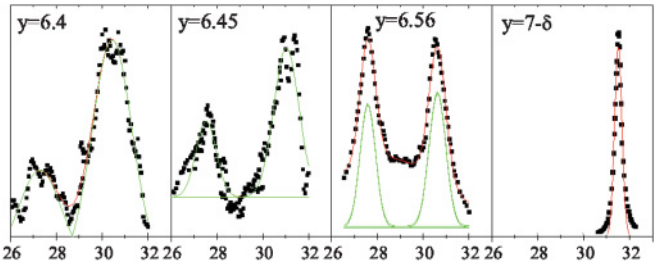

FIG. 3. (Color online) In-plane ^{63}Cu NQR frequency sweeps from Ref. 22.

oxygen superstructure with every second chain filled cannot be perfect away from $y = 6.5$. It is worth noting that holes go to the CuO_2 plane only at $y > 6.2$ [see Eq. (1)]. In the undoped case, $x = 0$, $y < 6.2$, there is only one NQR line with frequency $\nu_0 \approx 23.3$ MHz independent of y (see Ref. 23). By comparing ν_0 with frequencies of lines in Fig. 3 we see that the hole doping shifts the NQR frequency very strongly.[21] The present paper explains the significance of the chain-induced CDW for stability of the collinear antiferromagnetic phase at $x < 0.06$.

The structure of the paper is the following: The effective theory describing YBCO at low doping was formulated previously in Ref. 16. Section II summarizes ideas of the effective theory. In Sec. III the theory is applied to calculate reduction of the staggered magnetization in the antiferromagnetic phase at zero temperature. Temperature reduction of the staggered magnetization at zero and nonzero doping, $0 < x < 0.06$, is calculated in Sec. IV. Interplay between the chain-induced CDW, small hole pockets, and stability of the collinear antiferromagnetic phase is discussed in Sec. V. Section VI presents the conclusions of the paper.

II. EFFECTIVE LOW-ENERGY THEORY DESCRIBING LIGHTLY DOPED YBCO

This section summarizes the most important points of the effective low-energy theory suggested in Refs. 24 and 16 to describe YBCO at low doping. The analysis is based on the two-dimensional $t - t' - t'' - J$ model at small doping. The generic case of the single layer has been considered in Ref. 24. After integrating out the high-energy fluctuations one comes to the effective low-energy action of the model. The effective low-energy Lagrangian is written in terms of the bosonic $\vec{n}$ field ($n^2 = 1$) that describes the staggered component of the copper spins, and in terms of fermionic holons ψ. The term "holon" is used instead of "hole" to stress that spin and charge are to large extent separated (see Ref. 24). The holon has a pseudospin that originates from two sublattices, so the fermionic field ψ is the spinor in the pseudospin space. Minimums of the holon dispersion are at the nodal points $\mathbf{q}_0 = (\pm\pi/2, \pm\pi/2)$, so there are holons of two types corresponding to two pockets. The dispersion in a pocket is somewhat anisotropic, but for simplicity let us use here the isotropic approximation $\epsilon(\mathbf{p}) \approx \frac{1}{2}\beta\mathbf{p}^2$, where $\mathbf{p} = \mathbf{q} - \mathbf{q}_0$. The lattice spacing is set to be equal to unity, 3.81 Å $\rightarrow$ 1. All in all, the effective Lagrangian for

the single layer reads[24]

$$\mathcal{L} = \frac{\chi_\perp}{2}\dot{\vec{n}}^2 - \frac{\rho_s}{2}(\nabla\vec{n})^2 + \sum_\alpha \left\{ \frac{i}{2}[\psi_\alpha^\dagger \mathcal{D}_t \psi_\alpha - (\mathcal{D}_t\psi_\alpha)^\dagger \psi_\alpha] - \psi_\alpha^\dagger \epsilon(\mathcal{P})\psi_\alpha + \sqrt{2}g(\psi_\alpha^\dagger \vec{\sigma}\psi_\alpha)\cdot[\vec{n}\times(\boldsymbol{e}_\alpha\cdot\nabla)\vec{n}] \right\}. \quad (2)$$

The first two terms in the Lagrangian represent the usual nonlinear σ model. The magnetic susceptibility and the spin stiffness are $\chi_\perp \approx 0.53/8 \approx 0.066$ and $\rho_s \approx 0.175$.[25] Hereafter the antiferromagnetic exchange of the initial t-J model is set to be equal to unity,

$$J \approx 130\,\text{meV} \rightarrow 1.$$

Note that ρ_s is the bare spin stiffness; therefore by definition it is independent of doping. The rest of the Lagrangian in Eq. (2) represents the fermionic holon field and its interaction with the $\vec{n}$ field. The index $\alpha = a,b$ indicates the pocket in which the holon resides. The pseudospin operator is $\frac{1}{2}\vec{\sigma}$, and $\mathbf{e}_\alpha = (\pm 1/\sqrt{2}, 1/\sqrt{2})$ is a unit vector orthogonal to the face of the magnetic Brillouin zone (MBZ) where the holon is located. The argument of ϵ_α in Eq. (2) and the time derivative of the fermionic field in the same equation are "long" (covariant) derivatives,

$$\mathcal{P} = -i\nabla + \tfrac{1}{2}\vec{\sigma}\cdot[\vec{n}\times\nabla\vec{n}],$$
$$\mathcal{D}_t = \partial_t + \frac{i}{2}\vec{\sigma}\cdot[\vec{n}\times\dot{\vec{n}}].$$

The covariant derivatives reflect gauge invariance of the initial $t-t'-t''-J$ model.

Numerical calculations within the $t-t'-t''-J$ model with physical values of hopping matrix elements give the following values of the coupling constant and the inverse mass: $g \approx 1$, $\beta \approx 2.4$. The value of the inverse mass $\beta = 2.4$ corresponds to the effective mass $m^* = 1.8m_e$. The dimensionless parameter

$$\lambda = \frac{2g^2}{\pi\beta\rho_s} \quad (3)$$

plays the defining role in the theory. If $\lambda \leqslant 1$, the ground state corresponding to the Lagrangian (2) is the usual Néel state; the state is collinear at any small doping. If $1 \leqslant \lambda \leqslant 2$, the Néel state is unstable at arbitrarily small doping and the ground state is a static or a dynamic spin spiral. The wave vector of the spiral is

$$Q = \frac{g}{\rho_s}x. \quad (4)$$

If $\lambda \geqslant 2$, the system is unstable with respect to phase separation and/or charge-density-wave formation and hence the effective long-wavelength Lagrangian (2) becomes meaningless. The pure $t-J$ model ($t' = t'' = 0$) is unstable since it corresponds to $\lambda > 2$.

To find parameters of the effective action (2) one can rely on calculations within the $t-t'-t''-J$ model or alternatively, one can fit experimental data. Both approaches produce very close values of the parameters. The fit of elastic and inelastic neutron scattering data for $La_{2-x}Sr_xCuO_4$ performed in Ref. 24 gives the following values: $g = 1$, $\beta \approx 2.7$ ($m^* = 1.5\,m_e$), $\lambda \approx 1.30$. The fit of data on magnetic quantum oscillations in $YBa_2Cu_3O_y$ performed in Ref. 26 gives two possible sets:

$$g = 1,\ \beta = 2.78\ (m^* = 1.45\,m_e),\ \lambda = 1.31,$$
$$g = 1,\ \beta = 2.95\ (m^* = 1.35\,m_e),\ \lambda = 1.23. \quad (5)$$

These values are used in the present work.

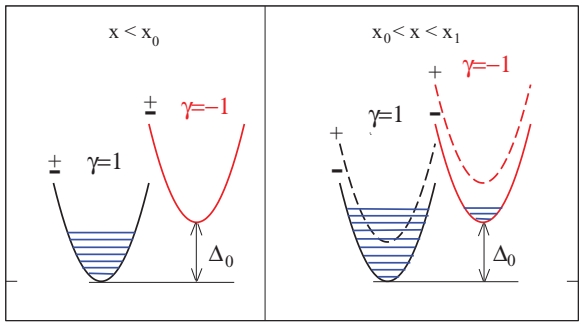

FIG. 4. (Color online) Filling of split holon bands in YBCO at $x < x_0$ (left) and $x > x_0$ (right). The solid and the dashed lines in the spin-spiral state, $x > x_0$, correspond to different pseudospin projections, and the splitting is $\pm gQ$. The doping x_1 indicated on the top of the right figure is $x_1 = 0.5x_0/(\lambda - 1)$ (see Ref. 16).

It is very easy to understand the reason for instability of the commensurate AF order under doping. Assuming such an order one can calculate the magnon Green's function

$$G(\omega,\boldsymbol{q}) \propto \frac{1}{\omega^2 - c^2q^2 - \mathcal{P}(\omega,\boldsymbol{q}) + i0}, \quad (6)$$

where $c = \sqrt{\rho_s/\chi_\perp} \approx 1.17\sqrt{2}J$ is the magnon speed in the parent Mott insulator, and $\mathcal{P}(\omega,\boldsymbol{q})$ is the fermionic polarization operator. A well-known peculiarity of the two-dimensional (2D) polarization operator is its independence of doping as soon as $\omega = 0$ and q is sufficiently small. A straightforward calculation gives at $q \rightarrow 0$, $\mathcal{P}(0,\boldsymbol{q}) = -\lambda c^2q^2$. Hence at $\lambda > 1$ the Stoner criterion in (6) is violated and the Green's function possesses poles at imaginary frequency, indicating instability of the AF ground state at an arbitrary small doping.

In YBCO the AF order is commensurate at $x < 0.06$; therefore the effective action (2) cannot be directly applied to this compound. To understand YBCO one can certainly assume that λ is doping dependent, $\lambda < 1$ at $x < 0.06$ and $\lambda > 1$ at $x > 0.06$. Purely theoretically it is hardly possible to have a significant x dependence of λ, but as a scenario one can consider this. However, in this scenario the incommensurate wave vector Q must jump from $Q = 0$ at $x < 0.06$ to Q given by Eq. (4) at $x > 0.06$. This is not consistent with data—there is no jump, and the incommensurate wave vector evolves smoothly above $x = 0.06$ (see Fig. 2).

A model describing the smooth evolution of Q with doping was suggested in Ref. 16. In addition to (2) the model incorporates two points. (i) Due to the bilayer structure the magnon spectrum in YBCO is split into acoustic and optic mode. The optic gap is about 70 meV;[27] hence the optic mode does not influence the low-energy dynamics, only acoustic magnons are important for these dynamics. (ii) The second point of the model is an assumption that the fermionic dispersion is split in two brunches as shown in Fig. 4 (left).

The splitting is Δ_0. The effective action that originates from (2) and incorporates these two points reads

$$\mathcal{L} = 2\times\left[\frac{\chi_\perp}{2}\dot{\vec{n}}^2 - \frac{\rho_s}{2}(\nabla\vec{n})^2\right] + \sum_{\alpha=a,b}\sum_{\gamma=\pm1}\left\{\frac{i}{2}[\psi^\dagger_{\alpha,\gamma}\mathcal{D}_t\psi_{\alpha,\gamma} - (\mathcal{D}_t\psi_{\alpha,\gamma})^\dagger\psi_{\alpha,\gamma}] - \psi^\dagger_{\alpha,\gamma}\left[\epsilon_\alpha(\mathcal{P}) - \gamma\frac{\Delta_0}{2}\right]\psi_{\alpha,\gamma} + \sqrt{2}g(\psi^\dagger_{\alpha,\gamma}\vec{\sigma}\psi_{\alpha,\gamma})\cdot[\vec{n}\times(\mathbf{e}_\alpha\cdot\nabla)\vec{n}]\right\}. \quad (7)$$

Compared to (2) the first line is multiplied by two, since the bilayer has the twice larger spin stiffness and magnetic susceptibility. In addition to the pocket index α, the holon field $\psi_{\alpha,\gamma}$ gets an additional index $\gamma = \pm1$ that indicates the branch of the split dispersion as it is shown in Fig. 4. Originally the paper[16] suggested that the hole band splitting $\gamma = \pm1$ was due to the hole hopping between layers inside the bilayer. So Δ_0 was the bonding-antibonding splitting. However, our recent analysis[28] indicates that antiferromagnetic correlations forbid the bonding-antibonding splitting. So, contrary to the assumption in Ref. 16, the interlayer hopping cannot contribute to Δ_0. In Sec. VI of the present paper I argue that the splitting Δ_0 is due to oxygen chains. For now let us accept the action (7) and study the consequences of this action.

When doping is sufficiently small,

$$x < x_0 = \frac{\Delta_0}{\pi\beta}, \quad (8)$$

only the $\gamma = 1$ band is populated [see Fig. 4 (left)]. In this case the fermionic polarization operator is half of that for the single-layer case: $\mathcal{P}(0,\boldsymbol{q}) = -\frac{1}{2}\lambda c^2q^2$, $q\to0$. Hence the Stoner stability criterion in Eq. (6) is fulfilled and the Néel order is stable. According to both neutron-scattering data[10,12,14] shown in Fig. 2 and to μSR data[9] shown in Fig. 1, the value of x_0 is $x_0 \approx 0.06$. Hence due to Eq. (8) the band splitting is

$$\Delta_0 \approx 0.5J \approx 65\ \text{meV}. \quad (9)$$

At $x > x_0$ fermions populate both $\gamma = 1$ and $\gamma = -1$ bands [Fig. 4 (right)], the polarization operator is doubled compared to the $x < x_0$ case, and the Stoner instability is there. As a result at $x > x_0$ the system develops the spiral with the wave vector,[16]

$$Q = \frac{g}{\rho_s}\frac{x - x_0}{3 - 2\lambda}. \quad (10)$$

The plot of $Q/2\pi$ versus doping is shown in Fig. 2 by the solid line. The development of the spin spiral is driven by the pseudospin splitting of the fermionic bands $\pm gQ$, as shown by the solid and dashed lines in Fig. 4 (right). Thus x_0 is a Lifshitz point, where the $\gamma = -1$ band starts to populate and where the spin spiral simultaneously starts to develop. In the present paper I consider quantum and thermal fluctuations in the Néel state, $x < x_0$. Quantum fluctuations in the spin spiral state at $x > x_0$ are considered separately.[29]

To summarize this section: The small hole pockets and associated spin spiral state are generic properties of all cuprates at low doping. The key point of the YBCO phenomenology is splitting of the hole pockets. This splitting together with splitting of magnon to the acoustic and the optic mode provides stability of the AF order up to 6%; doping.

III. QUANTUM FLUCTUATIONS IN THE NÉEL PHASE, REDUCTION OF THE ZERO-TEMPERATURE STAGGERED MAGNETIZATION

There are two magnons (two polarizations) in the Néel phase at $x < x_0$. The Green's function of each magnon reads

$$G(\omega,\boldsymbol{q}) = \frac{(2\chi_\perp)^{-1}}{\omega^2 - c^2q^2 - \mathcal{P}_0(\omega,\boldsymbol{q}) + i0}. \quad (11)$$

Only the $\gamma = 1$ band [see Fig. 4 (left)] contributes to the polarization operator $\mathcal{P}_0(\omega,\boldsymbol{q})$. Calculation of the polarization operator for the single layer was performed in Ref. 24. Comparing the single-layer action (2) and the double-layer action (7) and having in mind that at $x < x_0$ only the $\gamma = 1$ band is occupied, one immediately concludes that in the double-layer case the polarization operator is half of that calculated in Ref. 24. Hence

$$\begin{aligned}
&\text{Re}\,\mathcal{P}_0(\omega,\boldsymbol{q}) \\
&= -\frac{c^2g^2}{\pi\beta^2\rho_s}\Big\{\beta q^2 - R_1\sqrt{1 - R_0^2/R_1^2}\;\theta\big(1 - R_0^2/R_1^2\big) \\
&\quad - R_2\sqrt{1 - R_0^2/R_2^2}\;\theta\big(1 - R_0^2/R_2^2\big)\Big\}, \\
&\text{Im}\,\mathcal{P}_0(\omega,\boldsymbol{q}) = -\frac{c^2g^2}{\pi\beta^2\rho_s}\Big\{\theta\big(R_0^2 - R_1^2\big)\sqrt{R_0^2 - R_1^2} \\
&\qquad - \sqrt{R_0^2 - R_2^2}\,\theta\big(R_0^2 - R_2^2\big)\Big\}, \\
&R_0 = \beta q p_F, \quad R_1 = \frac{1}{2}\beta q^2 - \omega, \\
&R_2 = \frac{1}{2}\beta q^2 + \omega, \quad p_F = \sqrt{2\pi x}.
\end{aligned} \quad (12)$$

Here p_F is the Fermi momentum of the $\gamma = 1$ band and $\theta(x)$ is the usual step function. I've already pointed out above that at $q < 2p_F$, $\mathcal{P}_0(0,\boldsymbol{q}) = -\frac{\lambda}{2}c^2q^2$, so the Néel state is stable if $\lambda < 2$.

It is instructive to look at the magnon spectral function $-\text{Im}G(\omega,q)$ that describes inelastic neutron scattering. Spectral functions for $x = 0.05$ and for three values of the momentum q are plotted in Fig. 5 by solid lines. Spectral functions for both sets of parameters from Eq. (5) are almost identical. To be specific I present functions for the second set. In the same Fig. 5 the dashed lines show spectral functions in the parent Mott insulator [$\mathcal{P}_0(\omega,\boldsymbol{q}) = 0$]. The spectra demonstrate the low-energy incoherent part that absorbs more that 50%; of the spectral weight. The magnon quasiparticle peaks are still clearly pronounced. Their intensities are about half of that in the parent compound, and positions are slightly shifted up compared to the parent; the shift is proportional to the doping, $\delta\omega_q \propto x$. It is worth noting that while the reduction of the spectral weight is the reliable result, the upward shift is probably a byproduct of the low-energy effective theory. The effective theory accurately accounts for the magnon "repulsion" from the particle-hole continuum that is below the magnon. The "repulsion" results

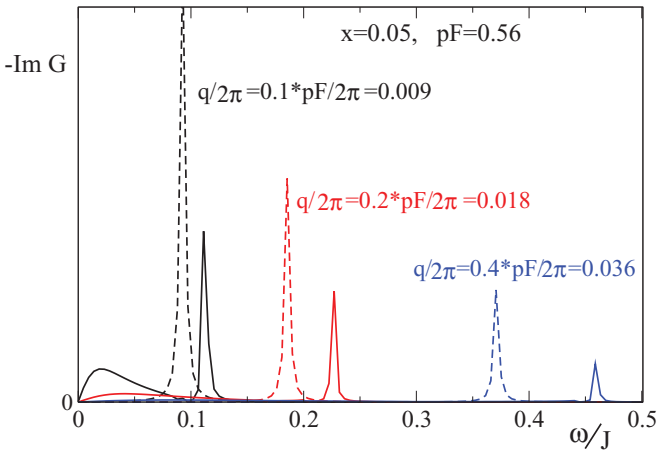

FIG. 5. (Color online) Solid lines show magnon spectral functions $-\mathrm{Im}G(\omega,q)$ versus ω for three values of momentum q and for doping $x = 0.05$. Dashed lines show spectral functions in the parent Mott insulator at the same values of momentum.

in the upward shift. However, there is also a "repulsion" from very-high-energy excitations ($E \sim 2t \sim 6J$) that are related to the incoherent part of the hole Green's function. This repulsion, unaccounted in the effective theory, leads to the downward shift of the magnon frequency that is also proportional to doping.[30] More generally one can say that the chiral effective field theory employed in the present work allows controllable calculations of effects that are x independent or scale as $\sqrt{x}$ or $x\ln(x)$. Quantities that scale as the first or as higher than first power of x are generally beyond the scope of the theory. Therefore at this stage one can say only that position of the magnon is approximately the same as that in the parent compound, but the magnon spectral weight is significantly reduced. Another point worth noting is the absence of the hourglass dispersion. The low-energy incoherent part of the Green's function clearly pronounced in Fig. 5 is transformed to the coherent hourglass only at $x > x_0$, beyond the Lifshitz point.[29]

Quantum fluctuation of the staggered magnetization is given by the standard formula

$$\langle n_\perp^2\rangle = -2\sum_{\mathbf{q}}\int\frac{d\omega}{2\pi i}G(\omega,\mathbf{q}) = -2\sum_{\mathbf{q}}\int\frac{d\omega}{2\pi}\mathrm{Im}G(\omega,\mathbf{q}). \tag{13}$$

The factor 2 comes from two polarizations. This expression must be renormalized by subtraction of the ultraviolet-divergent contribution that corresponds to the undoped σ model. The integral in (13) can be calculated analytically with logarithmic accuracy:

$$\langle n_\perp^2\rangle \approx \frac{\lambda\beta x}{4\rho_s}\ln\left(\frac{\Lambda}{p_F}\right) = \frac{\lambda\beta x}{8\rho_s}\ln\left(\frac{\Lambda^2}{\pi\beta x}\right). \tag{14}$$

There are two points to note: (i) In spite of the ultraviolet renormalization (σ-model subtraction), the fluctuation depends on the ultraviolet momentum cutoff $\Lambda \sim 1$. (ii) The leading logarithmic term, $x\ln(\Lambda^2/x)$, comes from momenta $p_F \ll q \ll \Lambda$.

The logarithm $\ln(\Lambda^2/x)$ is not large, and the logarithmic accuracy is not sufficient. Fortunately a numerical integration

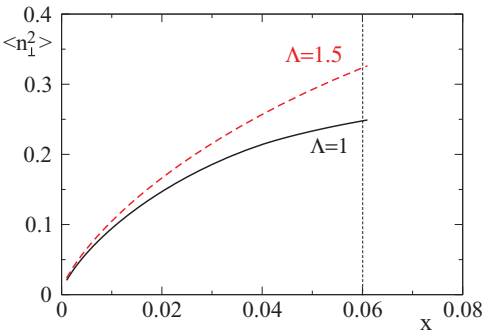

FIG. 6. (Color online) Quantum fluctuation $\langle n_\perp^2\rangle$ versus doping for two values of the ultraviolet cutoff Λ.

of (13) is straightforward. The result is presented in Fig. 6, where $\langle n_\perp^2\rangle$ is plotted versus doping. The second set of parameters from (5) is used, and results are presented for two values of the ultraviolet cutoff Λ. Reduction of the static component of the n field is $\langle n\rangle = \langle\sqrt{1-n_\perp^2}\rangle \approx 1 - \frac{1}{2}\langle n_\perp^2\rangle$. Hence the staggered magnetization is

$$\mu/\mu_B = 0.615\big(1 - \tfrac{1}{2}\langle n_\perp^2\rangle\big). \tag{15}$$

Here I take into account that the regularization procedure used corresponds to the normalization of the static component of the n field to unity at zero doping when the staggered magnetization is $0.615\mu_B$.[25] The plot of the calculated staggered magnetization μ versus doping together with experimental data[9] is presented in Fig. 1 (top). Dependence of the theoretical curve on Λ is pretty weak; to be specific, the curve corresponding to $\Lambda = 1$ is presented. Agreement between the theory and the experiment in the Néel phase is excellent. Thus, it is understood why quantum fluctuations only slightly reduce the staggered magnetization.

Note that the presented calculation is valid only in the Néel phase, $x < 0.06$. Physics in the spin-spiral phase, $x > 0.06$, is very much different because of the appearance of the soft "hourglass" dispersion and consequently, because of greatly enhanced quantum fluctuations. The corresponding results will be published separately.[29]

IV. TEMPERATURE DEPENDENCE OF THE STAGGERED MAGNETIZATION IN THE NÉEL PHASE

A. Zero doping

It is well known that due to the Mermin-Wagner theorem the Néel temperature in a spin-rotationally-invariant 2D system is exactly zero, $T_N = 0$. Cuprates are layered systems with a very small Heisenberg interaction, $J_\perp \lesssim 10^{-4}J$, between layers or bilayers. In spite of its smallness the interaction makes the system three dimensional, and hence it makes the Néel temperature finite, $T_N \sim J/\ln(J/J_\perp)$. Temperature dependence of the staggered magnetization in layered Heisenberg antiferromagnets has been intensively studied theoretically (for a review see Ref. 31). Unfortunately there is no a "small theoretical parameter" in the problem. Therefore while a qualitative behavior is absolutely clear, there is no universal quantitative description—different theoretical approaches give quite different results.[31] In the present section I develop an

effective description of the temperature dependence. This description certainly is not a rigorous solution of the layered Heisenberg antiferromagnet for all temperatures. This is a sort of interpolation between the $T \ll T_N$ regime and the $T \approx T_N$ regime. Importantly, the "interpolation" allows a quantitative description of an undoped layered Mott insulator, and much more importantly, it allows movement to the finite doping in the next subsection.

Let us start from the single-layer case (La_2CuO_4) and rewrite Eq. (13) in the Matsubara technique at a finite temperature:

$$\langle n_\perp^2 \rangle = \frac{2T}{\chi_\perp} \sum_{\mathbf{q}} \sum_s \frac{1}{\xi_s^2 + \omega_q^2}, \tag{16}$$

where $\omega_q = cq$ and $\xi_s = 2s\pi T$, $s = 0, \pm 1, \pm 2, \ldots$ is the Matsubara frequency. Hence the equation for $n_z = 1 - \frac{1}{2}\langle n_\perp^2 \rangle$ can be rewritten in the renormalization group (RG) form

$$\frac{dn_z}{n_z d\ln(q)} = \frac{T}{2\pi\rho_{sq}} \sum_s \frac{\omega_q^2}{\omega_q^2 + \xi_s^2}, \tag{17}$$

where $\rho_{sq} = \rho_s(q)$ is the q-dependent spin stiffness. Equation (17) assumes 2D geometry, so it is valid at $q > q_{\min}$, where the infrared cutoff $q_{\min} \propto \sqrt{J_\perp}$ is due to the Heisenberg coupling along the third dimension. To solve the RG problem one needs to add information on how the spin stiffness scales with the magnetization. Let us write the relation between the magnetization and the spin stiffness as

$$\frac{d\rho_{sq}}{\rho_{sq}} = r\frac{dn_z}{n_z}. \tag{18}$$

It is known[31] that one loop calculation valid at $n_z \approx 1$ results in $r = 1$ that implies $\rho \propto n_z$. On the other hand, close to the Néel temperature when $n_z \ll 1$ one should expect scaling very close to quadratic, $\rho \propto n_z^2$ ($r \approx 2$). This is because the critical index η of the magnon quasiparticle residue is very small (see, e.g., Refs. 32 and 33). For now I keep the power r as a parameter. Equations (17) and (18) are combined to

$$\frac{d\rho_{sq}}{d\ln(q)} = \frac{rT}{2\pi} \sum_s \frac{\omega_q^2}{\omega_q^2 + \xi_s^2}. \tag{19}$$

To perform the ultraviolet renormalization let us introduce ρ_Λ, the spin stiffness at the ultraviolet cutoff. Then due to Eq. (19) the finite temperature spin stiffness at $q = 0$ reads

$$\rho_{sT} = \rho_\Lambda - \frac{rT}{2\pi} \int_{q_{\min}}^{\Lambda} \left\{ \sum_s \frac{\omega_q^2}{\omega_q^2 + \xi_s^2} \right\} \frac{dq}{q}. \tag{20}$$

This expression can be renormalized by the condition that at zero temperature (more accurately, at $T \ll cq_{\min}$) the spin stiffness is equal the standard value $\rho_{s0} \approx 0.175J$ corresponding to the σ model originating from the spin-1/2 Heisenberg model. After the renormalization Eq. (20) is transformed to

$$\rho_{sT} = \rho_{s0} - \frac{rT}{2\pi} \int_{q_{\min}}^{\infty} \left\{ \sum_s \frac{\omega_q^2}{\omega_q^2 + \xi_s^2} - \frac{\omega_q}{2T} \right\} \frac{dq}{q}. \tag{21}$$

The three-dimensional interaction $J_\perp$ fixes the value of the infrared cutoff $q_{\min}$; however, one has to remember the scaling

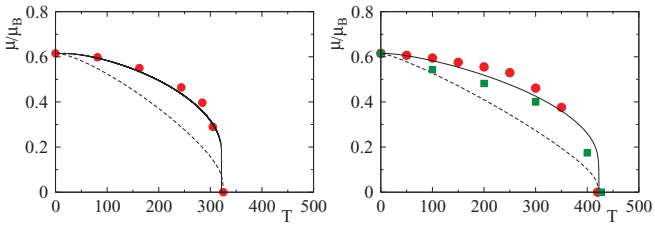

FIG. 7. (Color online) Staggered magnetization versus temperature in La_2CuO_4, left, and $YBa_2Cu_3O_6$, right. In the left plot red circles show neutron-scattering data.[34] In the right plot red circles show neutron-scattering data[35] and green squares show μSR data.[9] Theoretical curves with $r = 2$ are shown by solid lines, and theoretical curves with $r = 1$ are shown by dashed lines.

of the cutoff with the staggered magnetization n_z (see Ref. 31):

$$q_{\min} = q_{\min 0}\sqrt{n_z}, \tag{22}$$

where, due to (18),

$$n_z = \left[\frac{\rho_{sT}}{\rho_{s0}}\right]^{1/r}. \tag{23}$$

Equations (21), (22), and (23) can be easily integrated numerically. The Néel temperature is determined by zero spin stiffness (21). The infrared cutoff $q_{\min 0}$ is the only free parameter in the theory. The value of the parameter has to be tuned up to reproduce the measured Néel temperature. It has to be clear that $q_{\min 0}$ originates not only from $J_\perp$. Relativistic anisotropies such as Dzyaloshinskii-Moria, etc., also contribute to $q_{\min 0}$. Let us recall that due to the regularization procedure used the staggered magnetization is $\mu = 0.615\mu_B n_z$, where $0.615\mu_B$ is the the staggered magnetization in the parent Heisenberg model.[25] Staggered magnetization versus temperature in La_2CuO_4 (LCO) is presented in Fig. 7 (left). Red circles show neutron scattering data.[34] The theoretical curve with $r = 2$ and $q_{\min 0} = 0.024$ is shown by the solid line, and the theoretical curve with $r = 1$ and $q_{\min 0} = 0.004$ is shown by the dashed line. The curve with $r = 1$ corresponding to the single-loop RG describes the data very poorly. This illustrates the known problem of poor accuracy of the single-loop RG.[31] However, the curve with $r = 2$ corresponding to the critical scaling of the spin stiffness describes the data very well.

In the double-layer case (YBCO) the coefficient $\frac{rT}{2\pi}$ before the integral in Eq. (21) has to be replaced by the twice-smaller one, $\frac{rT}{4\pi}$. The point is that the optic magnon in YBCO has a gap of 70 meV and therefore it does not contribute to the low-energy dynamics. Only acoustic magnon is important; hence the effective number of magnons is twice smaller compared to LCO. Neutron-scattering data[35] for $YBa_2Cu_3O_6$ are shown in Fig. 7 (right) by red dots. Green squares show μSR data.[9] The theoretical curve with $r = 2$ and $q_{\min 0} = 0.0085$ is shown by the solid line and the theoretical curve with $r = 1$ and $q_{\min 0} = 0.0004$ is shown by the dashed line. Again, the curve with $r = 1$ is not consistent with the data. The curve with $r = 2$ is quite good.

It is worth noting that for both LCO and YBCO the values of the infrared cutoff $q_{\min 0}$ for $r = 1$ are unrealistically small, reflecting the same difficulty of single-loop RG (see also Ref. 31). On the other hand, the cutoff values for $r = 2$ are quite

reasonable, indicating that the Néel temperature is determined by spin-wave dynamics at distances up to $1/q_{\min 0} \sim 100$ lattice spacing along the plane.

All in all, the conclusion is that the effective RG developed in this section describes undoped compounds pretty well. To achieve this description one needs to set $r = 2$, which corresponds to the critical scaling of the spin stiffness expected in the vicinity of the Néel temperature, $\rho \propto n_z^2$. In the next section the developed description is applied to the nonzero doping case.

B. Nonzero doping

To extend to the finite doping case, one has to introduce in Eq. (21) the fermionic polarization operator:

$$\rho_{sT} = \rho_{s0} - \frac{rT}{2\pi}\int_{q_{\min}}^{\infty}\left\{\sum_s \frac{\omega_q^2}{\omega_q^2 + \xi_s^2 + \mathcal{P}_0(i\xi_s,q)} - \frac{\omega_q}{2T}\right\}\frac{dq}{q}, \tag{24}$$

where the polarization operator $\mathcal{P}_0(i\xi_s,q)$ is calculated at Matsubara frequencies. The expression for the polarization operator follows from the Lagrangian (7). One can use vertexes derived in Ref. 24 for the single-layer case and rescale the vertexes by a factor of $1/\sqrt{2}$, which follows from comparison of (2) and (7). The polarization operator reads

$$\begin{aligned}\mathcal{P}_0(i\xi,q) &= \pi\lambda c^2\beta q^2 \mathrm{Re}\sum_{\gamma=\pm1}\sum_{p}\frac{f_p^\gamma - f_{p+q}^\gamma}{\epsilon_p - \epsilon_{p+q} + i\xi}\\ &= 2\pi\lambda c^2\beta q^2 \mathrm{Re}\sum_{\gamma=\pm1}\sum_{p}\frac{f_p^\gamma}{\epsilon_p - \epsilon_{p+q} + i\xi}.\end{aligned} \tag{25}$$

Here f_p^γ is the Fermi-Dirac distribution function

$$f_p^\gamma = \frac{1}{e^{(\epsilon_p - \gamma\Delta_0/2 - \mu)/T} + 1}, \tag{26}$$

with chemical potential μ (do not mix it up with magnetic moment). Note that at $T \neq 0$ the $\gamma = -1$ band is also populated [see Fig. 4 (left)]. This is why the summation in (25) is performed over both bands, $\gamma = \pm 1$. The chemical potential is determined by the condition

$$2x = 2 \times 2\sum_{\gamma=\pm1}\sum_{p} f_p^\gamma, \tag{27}$$

which accounts for the double layer, the two pockets, and for the two pseudospin projections. It is easy to check that at zero temperature and at $q < 2p_F$ the zero-frequency polarization operator is $\mathcal{P}_0(0,q) = -\frac{\lambda}{2}\omega_q^2$, in agreement with the real frequency analysis at $x < x_0$ in Sec. III.

Numerical evaluation of the polarization operator (25) is straightforward. Substitution of the polarization operator in the RG Equation (24) and solution of this equation together with (22) and (23) gives staggered magnetization at a given doping and temperature. The RG equation is solved with $r = 2$ and $q_{\min 0} = 0.0085$, as it has been discussed in the previous subsection. These parameters are relevant to the n field and they are independent of doping. The fermionic polarization operator (25) is not very sensitive to the choice of parameters; to be specific, I present results corresponding to the second set of parameters in Eq. (5). The band splitting Δ_0 is determined by Eq. (9) which

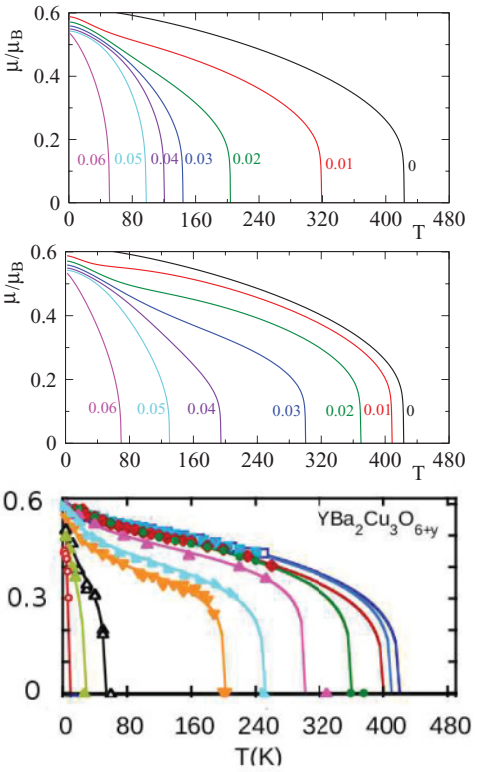

FIG. 8. (Color online) Staggered magnetization versus temperature in $YBa_2Cu_3O_y$ for several values of doping. Theoretical curves for $x = 0,0.1,0.2,0.3,0.4,0.5,0.6$ are shown in the top and middle panels. The top panel is obtained without account of the lifetime of the hole, $\Gamma = 0$. The mid panel is obtained with account of the hole lifetime. Experimental curves from Ref. 9 are presented in the bottom panel, and the doping levels are $x = 0.001$, 0.002, 0.005, 0.02, 0.029, 0.036, 0.039, 0.049, 0.061, 0.065.

is responsible for the position of the Lifshitz point, $x_0 = 0.06$. Plots of the staggered magnetization versus temperature for several values of doping are shown in the top panel in Fig. 8. Theoretical curves presented in the top panel are in a qualitative and to some extent quantitative agreement with data from Ref. 9 shown in Fig. 1 (bottom) and in Fig. 8 (bottom). The theory clearly demonstrates that while reductions of the zero-temperature staggered magnetization at $x < x_0$ are pretty small [Fig. 1 (top)], the reduction of the Néel temperature with doping is dramatic. There are two reasons for the reduction: (i) Thermal excitation of the precursor to the hourglass, the lower incoherent part of the magnetic spectrum shown in Fig. 5. (ii) Thermal population of the $\gamma = -1$ band. Figure 8 (top) indicates also some negative bending of $\mu(T)$ curves, in qualitative agreement with data presented in Fig. 8 (bottom).

Theoretical curves plotted in Fig. 8 (top) demonstrate even too steep a decrease of the Néel temperature with doping compared to experimental data shown in Fig. 1 (bottom). For example, at $x = 0.03$ the theoretical Néel temperature is 140 K [Fig. 8 (top)], while experimentally it is about 300 K [Fig. 1 (bottom)]. To fix this problem one has to realize that the above consideration of fermions disregards an important physical effect—the finite lifetime (scattering time) of a fermion at nonzero temperature. This is the same effect that

leads to the temperature-dependent resistivity. To understand the importance of this effect prior to calculations, one has to recall (see previous section) that the Néel temperature is formed at very large in-plane distances of up to 100 lattice spacings. This corresponds to $q \sim 0.01$ in Eqs. (24) and (25). The fermionic polarization operator at very small q (implying large distances) must depend on the fermion mean-free path. This explains the crucial importance of the fermion lifetime. To account for the lifetime effect, Eq. (25) has to be modified in the following way:

$$\mathcal{P}_0(i\xi,q) = 2\pi\lambda c^2\beta q^2 \sum_{\gamma=\pm1}\sum_{\boldsymbol{p}} \frac{(\epsilon_{\boldsymbol{p}}-\epsilon_{\boldsymbol{p}+\boldsymbol{q}})f_{\boldsymbol{p}}^{\gamma}}{(\epsilon_{\boldsymbol{p}}-\epsilon_{\boldsymbol{p}+\boldsymbol{q}})^2+\xi^2+\frac{\Gamma^2}{4}}. \tag{28}$$

Here Γ is the broadening due to scattering. Let us take the usual width characteristic for the two-dimensional Fermi liquid,[36]

$$\Gamma = A\frac{T^2}{\epsilon_F}, \tag{29}$$

where $\epsilon_F = \beta p_F^2/2 = \pi\beta x$ is the Fermi energy. I disregard the logarithmic T dependence of the coefficient A; the dependence is beyond accuracy of the calculation. The coefficient A will be used as a fitting parameter. Note that generally the width Γ depends on both temperature T and Matsubara frequency ξ_s. The dominating contribution to Eq. (24) comes from the zero Matsubara frequency. Therefore the width Γ is important in the zero-frequency term, $s = 0$, and it is completely negligible in $s \neq 0$ terms. Hence the width (29) corresponds to the zero Matsubara frequency. Numerical evaluation of the polarization operator (28) is not more difficult than evaluation of (25). Solution of the RG equations gives the staggered magnetization $\mu(T,x)$ with account of the fermion lifetime. The best fit of the experimental dependence of the Néel temperature on doping is achieved at

$$A \approx 0.7. \tag{30}$$

The calculated Néel temperature versus doping is shown by large red dots in Fig. 1 (bottom). The calculated staggered magnetization versus temperature is plotted in Fig. 8 (mid) for several values of doping. Experimental curves from Ref. 9 are presented in Fig. 8 (bottom). Overall agreement between theory and experiment is very good.

It is worth stressing again that the calculation of the temperature dependence of the magnetization in the layered system is less reliable than calculations of zero-temperature properties in Sec. III. The complexity of the finite-temperature case is due to the very large span of spacial scales involved in the problem, with the largest scale about 100 lattice spacings. Only leading effects have been taken into account in the present calculation. Clearly, there are subleading effects that also influence the magnetization. For example, usual disorder (impurities) must influence fermion dynamics at a scale of $\sim$100 lattice spacings and hence influence magnetization. In view of this comment, the agreement between theory and experimental data [see Fig. 1 (bottom) and Fig. 8 (middle)] is remarkable. Most importantly, the theory explains why the Néel temperature drops down dramatically with doping, while the zero-temperature magnetization is almost doping independent. This "contradictory" behavior is due to the band splitting and due to different fillings of the split bands. The different filling is a fingerprint of small hole pockets. At zero temperature only the lower band is occupied, while temperature populates the upper band as well. The "contradictory" behavior is closely related to the Lifshitz point at $x = x_0$ and to the development of the spin spiral at $x > x_0$ when both bands are occupied at zero temperature.

V. CDW INDUCED BY OXYGEN CHAINS, SMALL HOLE POCKETS, MECHANISM FOR BAND SPLITTING

The key point of the YBCO phenomenology suggested in Ref. 16 and applied in the present work is the splitting of hole bands. There are other key points, like small hole pockets, spin spirals, etc. However, these other points are not specific to YBCO, they are generic for all cuprates. The band splitting is specific to YBCO. The paper[16] suggested that the hole band splitting in YBCO was due to the hole hopping between layers inside the bilayer, the bonding-antibonding splitting. However, our recent analysis[28] indicates that antiferromagnetic correlations *between* the layers forbid the bonding-antibonding splitting. If the hole hopping matrix element between the layers is $t_\perp$, then the band splitting in the case of AF correlations between the layers is $\propto t_\perp(\cos k_x + \cos k_y)$ [see Ref. 28]. The splitting is zero at the nodal points $(k_x,k_y) = (\pm\pi/2, \pm\pi/2)$, contrary to the assumption (7).

Thus, contrary to the assumption in Ref. 16, the interlayer hopping cannot contribute to Δ_0. Another mechanism for splitting is necessary. In this section I argue that the splitting is due to oxygen chains. Let us first consider the case $y = 6.5$ when every second chain is fully filled. In this case chains produce the effective pseudopotential for in-plane holes

$$V_c(X) = -v_0\cos(\pi X), \tag{31}$$

where v_0 is the amplitude of the potential and X is the direction perpendicular to chains. (I denote the distance by capital X to make it different from the doping x.) The hole dispersion in the antiferromagnetic background is shown in Fig. 9. The dispersion consists of two full pockets, the pocket a and the pocket b. There is the perfect nesting condition between the pockets and the chain potential (31), and therefore the two split bands are generated:

$$\epsilon_p = -v_0 + \frac{\beta}{2}p^2\ ,\ \psi_+ = \frac{|a\rangle_p + |b\rangle_p}{\sqrt{2}} \propto \cos\left(\frac{\pi}{2}X\right)e^{i\boldsymbol{p}\cdot\boldsymbol{r}},$$
$$\epsilon_p = +v_0 + \frac{\beta}{2}p^2\ ,\ \psi_- = \frac{|a\rangle_p - |b\rangle_p}{\sqrt{2}} \propto \sin\left(\frac{\pi}{2}X\right)e^{i\boldsymbol{p}\cdot\boldsymbol{r}}. \tag{32}$$

Here $\boldsymbol{p}$ is the momentum with respect to the center of the pocket. Equations (32) represent exactly the $\gamma = \pm1$ band splitting adopted in (7). Due to the exact nesting of small hole pockets, a tiny pseudopotential $v_0 \approx 30$ meV is sufficient to generate the splitting $\Delta_0 = 2v_0 \approx 65$ meV that follows from the magnetic analysis [see Eq.(9)].

There might be an impression that the splitting (32) is not quite equivalent to the effective action (7). For example, the question arises why there is no a spin-wave vertex that transfers ψ_+ to ψ_-? The vertex carries a large momentum π, and therefore the vertex vanishes after integration over X. In other words, soft magnons included in the effective action (7)

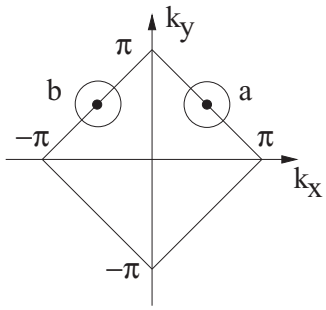

FIG. 9. Single-hole dispersion in the AF background.

cannot induce a transition with the large momentum transfer. Careful analysis shows that the splitting (32) with account of two layers is completely equivalent to (7).

According to (32), the wave function of the lower $\gamma = +1$ band is nonzero at $X = 0,2,4,...$ while the wave function of the upper $\gamma = -1$ band is nonzero at X= 1,3,5,... Due to the splitting the bands are differently populated, and this results in the in-plane hole density wave with a period of the two lattice spacing.[19,20] Let us calculate the amplitude of the CDW. The oxygen content $y = 6.5$ corresponds to doping $x \approx 0.1$ [see Eq. (1)]. This doping is within the spin-spiral phase; therefore to calculate fillings of bands one has to account the spin spiral as it is shown in Fig. 4 (right). In the lower $\gamma = +1$ band both pseudospin projections are populated, while in the upper $\gamma = -1$ band only one pseudospin projection is populated. Populations of different subbands have been calculated in the analysis of magnetic quantum oscillations [see Eqs. (4) in Ref. 26]. From these equations one concludes that populations of the upper and lower bands ($\gamma = \mp 1$) are

$$x_{-1} = \frac{2-\lambda}{2(3-2\lambda)}(x - x_0), \qquad x_{+1} = x - x_{-1}. \tag{33}$$

Naturally, the population of the upper band vanishes at $x = x_0$; this is the Lifshitz point. For $x = 0.1, x_0 = 0.06$, and $\lambda = 1.23$, one finds $x_{-1} = 0.03$ and $x_{+1} = 0.07$. Hence the hole density per cite at every even value of X is $2x_{+1} = 0.14$ and at every odd value of X it is $2x_{-1} = 0.06$. However, this is not the amplitude of the CDW yet.

All equations in the present paper are written in terms of holes dressed by magnetic quantum fluctuations (magnetic polarons). Hence $x_{\pm 1}$ are densities of the *dressed holes*. The dressed hole has a finite size; therefore, the charge-density modulation is smaller than that naively given by $x_{\pm 1}$. It is known that the quasiparticle residue of the dressed hole is about $Z \approx 0.4$ (see, e.g., Ref. 37). This means that with the probability $Z \approx 0.4$ the hole resides at the same site as the quasihole, and with the probability $(1 - Z)/4 \approx 0.15$ the hole resides at each of the four nearest Cu sites. Therefore the real charge densities per site are

$$\rho_{+1} = 2\left[\left(Z + 2\frac{1-Z}{4}\right)x_{+1} + 2\frac{1-Z}{4}x_{-1}\right] \approx 0.12,$$
$$\rho_{-1} = 2\left[\left(Z + 2\frac{1-Z}{4}\right)x_{-1} + 2\frac{1-Z}{4}x_{+1}\right] \approx 0.08. \tag{34}$$

This gives the amplitude of the CDW. The estimate of the amplitude is basedpurely on magnetic data. It depends mainly on the position of the Lifshitz point, $x_0 = 0.06$.

NQR was not used in the estimate (34). Nevertheless the estimate is pretty much consistent with NQR data[22] presented in Fig. 3. The NQR frequency shift with respect to the frequency of the undoped sample, $\nu_0 = 23.3$ MHz,[23] is proportional to the local hole concentration[21]

$$\nu_Q = 23.3 \text{ MHz} + B\rho. \tag{35}$$

The higher frequency NQR line at $y = 6.56$ is $\nu_2 \approx 30.3$ MHz (see Fig. 3). According to Eq. (34), the line corresponds to $\rho \approx 0.12$. Hence the constant B in Eq. (35) is $B \approx 58$ MHz/hole. Interestingly, the value of B is significantly larger than that in $La_{2-x}Sr_xCuO_4$, $B \approx 20$ MHz/hole,[21] and in $HgBa_2CuO_{4+\delta}$, $B \approx 30$ MHz/hole.[38] Assuming that optimal doping corresponds to $\rho \approx 0.14$ and using Eq. (35), one finds the optimal doping NQR frequency $\nu = 31.4$ MHz. This value is pretty close to $\nu_{\text{opt}} \approx 31.6$ MHz, which follows from Fig. 3 at $y \approx 7$. According to (34) the lower frequency NQR line at $y \approx 6.5$ corresponds to $\rho \approx 0.08$. Substituting this value in Eq. (35), one finds the frequency $\nu = 27.9$ MHz. Again, this value is pretty close to the lower frequency line $\nu_1 \approx 27.8$ MHz that is shown in Fig. 3 at $y = 6.56$. Thus the amplitude of the CDW determined from the position of the Lifshitz point is fully consistent with the NQR data.

The simple potential (31) is literally applicable only to $y = 6.5$. Obviously, there is no any modulation at $y = 7$ as the rightmost Fig. 3 indicates. Away from $y = 6.5$ more complex oxygen superstructures can appear.[39] An assumption important for the present work is that at $0 < x < 0.1$ ($6.20 < y < 6.5$) the superstructure (31) is dominating. NQR data[22] for $y = 6.4$ and $y = 6.45$ presented in Fig. 3 support this assumption: there are only two NQR lines that are only slightly broader than the lines at $y = 6.5$.

VI. CONCLUSIONS

Small hole pockets and the associated spin spiral state are generic properties of all cuprates at low doping. The key point of the YBCO phenomenology additional to the generic properties is splitting of the hole pockets into the lower band and the upper band. This splitting together with splitting of magnon to the acoustic and the optic mode provides stability of the collinear aniferromagnetic order at doping below the Lifshitz point at $x \approx 0.06$. At doping below the Lifshitz point only the lower band is populated. At higher doping the upper band starts to populate and simultaneously the spin spiral starts to develop.

At doping below the Lifshitz point the doping-induced spin quantum fluctuations are pretty weak. This explains why the zero-temperature staggered magnetization is close to $0.6\mu_B$, the maximum value allowed by quantum fluctuations of localized spins. The developed theory perfectly reproduces the weak decrease of the staggered magnetization with doping observed experimentally.

While the zero-temperature staggered magnetization is almost doping independent, the Néel temperature decays very quickly from $T_N = 420$ K at $x = 0$ to practically zero at $x \approx 0.06$. This quick decay is a consequence of the closeness

to the Lifshitz point. Again, the theory reproduces very well the doping dependence of the Néel temperature as well as the observed temperature dependence of the staggered magnetization at a given doping.

The band splitting (the hole pocket splitting) is induced by the modulation of oxygen chains. The main period of the modulation is two lattice spacings. Because of the perfect nesting between the small hole pockets and the period of the modulation, a small pseudopotential caused by the chains is sufficient to induce the band splitting at about 60 meV. The splitting causes the in-plane charge-density wave with a significant amplitude dependent on doping.

ACKNOWLEDGMENTS

I am grateful to W. Chen, J. Haase, M.-H. Julien, A. A. Katanin, G. Khaliullin, D. Manske, W. Metzner, A. I. Milstein, R. De Renzi, S. Sanna, T. Tohyama, and C. Ulrich for important stimulating discussions and comments. The main part of this work was done during my stay at the Max Planck Institute for Solid State Research, Stuttgart,and the Yukawa Institute, Kyoto.I am very grateful to my colleagues for hospitality and for the stimulating atmosphere. This work was supported by the Humboldt Foundation and by the Japan Society for the Promotion of Science.

[1] Y. Wang and N. P. Ong, Proc. Natl. Acad. Sci. USA **98**, 11091 (2001).

[2] X. F. Sun, K. Segawa, and Y. Ando, Phys. Rev. B **72**, 100502R (2005).

[3] N. Doiron-Leyraud, M. Sutherland, S. Y. Li, L. Taillefer, R. Liang, D. A. Bonn, and W. N. Hardy, Phys. Rev. Lett. **97**, 207001 (2006).

[4] M. Sutherland, S. Y. Li, D. G. Hawthorn, R. W. Hill, F. Ronning, M. A. Tanatar, J. Paglione, H. Zhang, L. Taillefer, J. DeBenedictis, R. Liang, D. A. Bonn, and W. N. Hardy, Phys. Rev. Lett. **94**, 147004 (2005).

[5] G. S. Boebinger, Y. Ando, A. Passner, T. Kimura, M. Okuya, J. Shimoyama, K. Kishio, K. Tamasaku, N. Ichikawa, and S. Uchida, Phys. Rev. Lett. **77**, 5417 (1996).

[6] Y. Ando, K. Segawa, S. Komiya, and A. N. Lavrov, Phys. Rev. Lett. **88**, 137005 (2002).

[7] $La_{2-x}Sr_xCuO_4$ is a superconductor at $x > 0.055$, but still it is an Anderson insulator from the point of view of the single-particle physics.

[8] R. Liang, D. A. Bonn, and W. N. Hardy, Phys. Rev. B **73**, 180505(R) (2006).

[9] F. Coneri, S. Sanna, K. Zheng, J. Lord, and R. De Renzi, Phys. Rev. B **81**, 104507 (2010).

[10] V. Hinkov, P. Bourges, S. Pailhes, Y. Sidis, A. Ivanov, C. D. Frost, T. G. Perring, C. T. Lin, D. P. Chen, and B. Keimer, Nature Phys. **3**, 780 (2007).

[11] C. Stock, W. J. L. Buyers, Z. Yamani, Z. Tun, R. J. Birgeneau, R. Liang, D. Bonn, and W. N. Hardy, Phys. Rev. B **77**, 104513 (2008).

[12] V. Hinkov, D. Haug, B. Fauque, P. Bourges, Y. Sidis, A. Ivanov, C. Bernhard, C. T. Lin, and B. Keimer, Science **319**, 597 (2008).

[13] V. Hinkov, S. Pailhes, P. Bourges, Y. Sidis, A. Ivanov, A. Kulakov, C. T. Lin, D. P. Chen, C. Bernhard, and B. Keimer, Nature **430**, 650 (2004).

[14] C. Stock, W. J. L. Buyers, R. Liang, D. Peets, Z. Tun, D. Bonn, W. N. Hardy, and R. J. Birgeneau, Phys. Rev. B **69**, 014502 (2004).

[15] D. Haug, V. Hinkov, Y. Sidis, P. Bourges, N. B. Christensen, A. Ivanov, T. Keller, C. T. Lin, and B. Keimer, New J. Phys. **12**, 105006 (2010).

[16] O. P. Sushkov, Phys. Rev. B **79**, 174519 (2009).

[17] T. Tohyama, Phys. Rev. B **70**, 174517 (2004).

[18] Commensurate antiferromagnetism in $La_{2-x}Sr_xCuO_4$ survives up to $x = 0.02$ only due to strong localization of holes; holes are immobile.

[19] Z. Yamani, W. A. MacFarlane, B. W. Statt, D. Bonn, R. Liang, and W. N. Hardy, Physica C **405**, 227 (2004).

[20] D. L. Feng, A. Rusydi, P. Abbamonte, L. Venema, I. Elfimov, R. Liang, D. A. Bonn, W. N. Hardy, C. Schusler-Langeheine, S. Hulbert, C.-C. Kao, and G. A. Sawatzky, e-print arXiv:cond-mat/0402488.

[21] J. Haase, O. P. Sushkov, P. Horsch, and G. V. M. Williams, Phys. Rev. B **69**, 094504 (2004).

[22] R. Ofer and A. Keren, Phys. Rev. B **80**, 224521 (2009).

[23] P. Mendels, H. Alloul, J. F. Marucco, J. Arabski, and G. Collin, Physica C **171**, 429 (1990).

[24] A. I. Milstein and O. P. Sushkov, Phys. Rev. B **78**, 014501 (2008).

[25] R. R. P. Singh, Phys. Rev. B **39**, 9760 (1989); Z. Weihong, J. Oitmaa, and C. J. Hamer, *ibid.* **43**, 8321 (1991).

[26] W. Chen, O. P. Sushkov, and T. Tohyama, Phys. Rev. B **82**, 060511(R) (2010).

[27] D. Reznik, P. Bourges, H. F. Fong, L. P. Regnault, J. Bossy, C. Vettier, D. L. Milius, I. A. Aksay, and B. Keimer, Phys. Rev. B **53**, R14741 (1996); S. M. Hayden, G. Aeppli, T. G. Perring, H. A. Mook, and F. Dogan, *ibid.* **54**, R6905 (1996).

[28] W. Chen, O. P. Sushkov, and T. Tohyama, e-print arXiv:1108.4002 (to be published).

[29] A. I. Milstein and O. P. Sushkov (to be published).

[30] G. Khaliullin and P. Horsch, Phys. Rev. B **47**, 463 (1993).

[31] A. A. Katanin and V. Yu. Irkhin, Phys. Usp. **50**, 613 (2007).

[32] A. V. Chubukov, S. Sachdev, and J. Ye, Phys. Rev. B **49**, 11919 (1994).

[33] V. Yu. Irkhin and A. A. Katanin, Phys. Rev. B **55**, 12318 (1997).

[34] B. Keimer, A. Aharony, A. Auerbach, R. J. Birgeneau, A. Cassanho, Y. Endoh, R. W. Erwin, M. A. Kastner, and G. Shirane, Phys. Rev. B **45**, 7430 (1992).

[35] J. Rossat-Mignod, P. Burlet, M. J. Jurgens, C. Vettier, L. P. Regnault, J. Y. Henry, C. Ayache, L. Forro, H. Noel, M. Potel, P. Gougeon, and J. C. Levet, J. Phys. (Paris), Colloq. **49**, C8-2119 (1988).

[36] J. Jackeli and V. Yu. Yushankhai, Phys. Rev. B **56**, 3540 (1997).

[37] O. P. Sushkov, G. A. Sawatzky, R. Eder, and H. Eskes, Phys. Rev. B **56**, 11769 (1997).

[38] Wei Chen, G. Khaliullin, and O. P. Sushkov, Phys. Rev. B **83**, 064514 (2011).

[39] J. Strempfer, I. Zegkinoglou, U. Rutt, M. v. Zimmermann, C. Bernhard, C. T. Lin, Th. Wolf, and B. Keimer, Phys. Rev. Lett. **93**, 157007 (2004).